JGR Oceans

RESEARCH ARTICLE
10.1029/2019JC015870

Key Points:
- For reef topography, which is multiscale, a wide range of length scales contribute substantially to the frontal area per unit plan area
- Representing reef topography as an obstacle array does not capture the substantial contribution of small length scales to total frontal area
- Method is proposed for computing roughness density from local surface slopes that includes contributions from all topographic length scales

Supporting Information:
- Supporting Information S1

Correspondence to:
M. S. Duvall,
melissa.duvall@duke.edu

Citation:
Duvall, M. S., Rosman, J. H., & Hench, J. L. (2020). Estimating geometric properties of coral reef topography using obstacle- and surface-based approaches. *Journal of Geophysical Research: Oceans*, *125*, e2019JC015870. https://doi.org/10.1029/2019JC015870

Received 11 NOV 2019
Accepted 23 MAY 2020
Accepted article online 29 MAY 2020

Estimating Geometric Properties of Coral Reef Topography Using Obstacle- and Surface-Based Approaches

Melissa S. Duvall[1], Johanna H. Rosman[2], and James L. Hench[1]

[1]Marine Laboratory, Nicholas School of the Environment, Duke University, Beaufort, NC, USA, [2]Institute of Marine Sciences, University of North Carolina at Chapel Hill, Morehead City, NC, USA

Abstract In shallow water systems like coral reefs, bottom friction is an important term in the momentum balance. Parameterizations of bottom friction require a representation of canopy geometry, which can be conceptualized as an array of discrete obstacles or a continuous surface. Here, we assess the implications of using obstacle- and surface-based representations to estimate geometric properties needed to parameterize drag. We collected high-resolution reef topography data using a scanning multibeam sonar that resolved individual coral colonies within a set of 100-m^2 reef patches primarily composed of mounding *Porites* corals. The topography measurements yielded 1-cm resolution continuous surfaces consisting of a single elevation value for each position in a regular horizontal grid. These surfaces were analyzed by (1) defining discrete obstacles and quantifying their properties (dimensions, shapes), and (2) computing properties of the elevation field (root mean square (rms) elevations, rms slopes, spectra). We then computed the roughness density (i.e., frontal area per unit plan area) using both analysis approaches. The obstacle and surface-based estimates of roughness density did not agree, largely because small-scale topographic variations contributed significantly to total frontal area. These results challenge the common conceptualization of shallow-water canopies as obstacle arrays, which may not capture significant contributions of high-wavenumber roughness to total frontal area. In contrast, the full range of roughness length scales present in natural reefs is captured by the continuous surface representation. Parameterizations of bottom friction over reef topography could potentially be improved by representing the contributions of all length scales to total frontal area and drag.

Plain Language Summary Coral reefs depend on water motion for survival. At the same time, their complex structure exerts friction on the overlying flow and thereby affects water movement across reefs. Prediction of flow over reefs requires a model that captures the interaction between reef topography and the flow. This is typically done with a drag law that requires specification of the frontal area of topography perpendicular to the flow per unit horizontal area. Quantifying frontal area is problematic because reef topography has many length scales. Here we consider the effect that representing reefs either as discrete obstacle arrays (e.g., cylinders) or as continuous rough surfaces (e.g., represented by spectra) has on estimates of frontal area and drag. Our results show that the obstacle representation misses the contribution of small length scales while the surface approach captures all length scales, which contribute significantly to the total frontal area of natural reefs. This suggests that the many different topographic length scales should be considered in models of friction for flow across reefs.

1. Introduction

In coastal systems such as coral reefs, bottom stress is often an important term in the momentum budget. Predicting circulation in these systems therefore requires adequate parameterization of bottom friction. Development of friction models for flow over reefs is difficult because the relationship between the drag force on the flow and the physical characteristics of the complex bottom is not well understood (Monismith, 2007).

As water moves over complex reef topography, the primary mechanism by which energy is removed from currents and waves is via form drag. Form drag arises due to pressure differences across obstacles in the flow and results in conversion of mean flow kinetic energy to turbulent kinetic energy. In high Reynolds number, separated flows, form drag is typically well described by a quadratic drag law that relates the drag force to the

flow speed squared. This relationship can be expressed per unit plan bottom area as (e.g., Wooding et al., 1973)

$$\frac{F_d}{A_T} = \tau_{\text{eff}} = \frac{1}{2} c_d \lambda_f U^2 \quad (1)$$

Here, τ_{eff} is the effective bottom stress defined as the drag force F_d per unit bottom area A_T, λ_f is the frontal area of solid obstacles seen by the flow per unit plan bottom area and is often referred to as the roughness density, U is a representative current speed for flow through the canopy, and c_d is a drag coefficient. If the water depth is much larger than the height of roughness elements, a boundary layer forms above the topography in which the velocity profile shape is affected by turbulence generated at the bottom, typically represented via a roughness length-scale z_0 (Reidenbach et al., 2006). Laboratory flume studies and numerical simulations of flow over obstacle arrays have shown that z_0 varies with both roughness element size and λ_f (Coceal & Belcher, 2004; Lettau, 1967, 1969; MacDonald et al., 1998). The roughness density, λ_f, is therefore an important geometric property for representing effects of topography on flow.

In previous work that quantified bottom friction on reefs, the drag force per unit bottom area has been deduced from the spatially averaged momentum budget (e.g., Lentz et al., 2017; Lentz et al., 2018; McDonald et al., 2006), or measurements in the bottom boundary layer above reefs (e.g., Reidenbach et al., 2006). While these approaches yield estimates of the total drag force per unit bottom area, they cannot be used in a predictive way to estimate the drag force for a new reef geometry. Asher et al. (2016) and Samuel and Monismith (2013) measured the drag force on coral skeletons directly in laboratory flumes. By combining information about the total drag force and velocity incident on the corals, they were able to estimate $c_d\lambda_f$. Information about λ_f then allowed c_d to be estimated. Estimation of the drag force using Equation 1 relies on knowing both c_d and λ_f, together with the velocity of water that interacts with the reef topography. Although c_d varies across a reef, previous studies suggest that spatially averaged c_d is of order unity (e.g., Asher et al., 2016), while λ_f can vary over orders of magnitude depending on reef geometry. Although λ_f is an important geometric property for representing the effects of topography on flow, little attention has been given to estimating frontal area for natural reefs.

To quantify λ_f in other systems, studies have conceptualized and modeled complex topography as either (1) an array of discrete obstacles that typically have uniform geometry; or (2) a continuous surface of normally distributed elevation (Grinvald & Nikora, 1988). The discrete obstacle representation has been applied to small-scale bedforms (Kean & Smith, 2006a, 2006b) and emergent and near-emergent vegetation (Finnigan, 2000; Nepf, 1999; Nepf & Vivoni, 2000; Raupach & Thom, 1981), as well as urban canopies and terrestrial forests where the obstacle layer is a small part of a much larger boundary layer (Coceal & Belcher, 2004; Di Sabatino et al., 2008; Kutzbach, 1961; MacDonald et al., 1998). Coral reef topography has been represented as regular cylinder arrays (Lowe et al., 2005, 2007) and regular hemisphere arrays (Yu et al., 2018), making quantification of frontal area simple. While these studies have greatly advanced our understanding of the physics of canopy flows and rough boundary layers, the effects of the range of roughness length scales present on real reefs are unclear.

Complex topography has also been represented as a surface of elevation values, quantified using moments of the distribution (Duvall et al., 2019; Lowe et al., 2005) or the spectral density of the surface (Nunes & Pawlak, 2008; Zawada & Brock, 2009). Surface representations capture a range of length scales and have shown that coral topography is both multiscale and multifractal (Duvall et al., 2019). Coral topography has been modeled as a single sinusoid (Rogers et al., 2018), but this represents only a single length scale. Reefs have also been modeled as fractal processes with self-affine scaling behavior (Purkis & Kohler, 2008; Zawada & Brock, 2009); however, these models assume that the elevation is normally distributed and capture only a single scaling behavior.

Regardless of the reef properties and choice of representation, accurately modeling circulation over reefs depends on our ability to quantify λ_f. To our knowledge, no previous attempts have been made to quantify λ_f by representing natural reef topography as either an obstacle array or a continuous surface, or to compare the two approaches. Here, we characterize important properties of natural reef topography measured using a high-resolution multibeam scanning sonar system. This study is the first to compare λ_f estimates based on obstacle and surface properties, which is needed to improve our understanding of drag (Napoli

et al., 2008). We also evaluate the ability of previously proposed obstacle and surface models to represent a complex reef populated by mounding coral (*Porites*), and present recommendations for representing topography in bottom friction parameterizations for circulation models.

2. Roughness Density From Obstacle- and Surface-Based Approaches

The roughness density λ_f represents the total frontal area "seen" by the flow, A_f, divided by the corresponding horizontal plan area, A_T (Lettau, 1969). This can be computed from the frontal areas of discrete obstacles within a patch of reef, or by integrating vertical elevation changes in the continuous surface. Both approaches can capture multiple horizontal and vertical roughness length scales and are equivalent for arrays of smooth, distinct obstacles, such as isolated Gaussian humps. However, it is uncertain whether obstacle and surface-based roughness density estimates are equivalent for multiscale natural topography.

2.1. Topography as a Three-Dimensional Obstacle Array

To calculate frontal area by representing topography as an array of obstacles, each distinct obstacle must first be identified. The frontal area of each obstacle was computed from the maximum obstacle width in the cross-flow direction at specified heights above the seafloor. The approach used in the present study to identify obstacles in reef topography and compute frontal area is detailed in section 3.2.

For an array of distinct obstacles with uniform shapes but variable size, the frontal area per unit plan area can be calculated from the vertical and horizontal length scales of the roughness elements as

$$\lambda_{f,o} = \frac{\alpha \sum_{i=1}^{N} l_{x,i} l_{z,i}}{L_x L_y}, \tag{2}$$

where $l_{x,i}$ and $l_{z,i}$ are the cross-flow width and height of the i^{th} roughness element in the array, N is the total number of elements, and L_x and L_y are the side lengths of the patch, such that $A_T = L_x L_y$. The coefficient α is a shape factor of order unity that relates the product of length scales to the cross-sectional area. For example, for cylinders $\alpha = 1$ and for semispheroid obstacles $\alpha = \pi/4$.

2.2. Topography as a Two-Dimensional Continuous Surface

For reef topography that can be described by a single-valued function of horizontal coordinates, $f(x, y)$, the roughness density for flow in the y direction can be computed as

$$\lambda_{f,s} = \frac{1}{L_x L_y} \int_0^{L_x} \int_0^{L_y} \left(\frac{\partial f}{\partial y} \right)_{pos} \mathrm{d}y \, \mathrm{d}x, \tag{3}$$

where $\partial f/\partial y$ is the local bottom slope in the along-flow (y) direction, which is only included in the sum if $\partial f/\partial y$ at the point (x, y) is positive. If the frequency distribution of bottom slope is symmetric about $\partial f/\partial y = 0$, the integral can instead be evaluated as the integral of absolute value of slope over all slope values and the total divided by 2. This is related to the effective slope, *ES,* defined in some previous studies such that $ES = 2\lambda_{f,s}$ (Napoli et al., 2008; Stewart et al., 2019).

Some previous studies have modeled reef topography as a one-dimensional sinusoid with a single amplitude (b) and wavelength (Λ), by matching the observed rms slope, $(\mathrm{d}f/\mathrm{d}y)_{\mathrm{rms}}$, with that for a sine wave (Rogers et al., 2018). In this case, $\lambda_{f,s}$ can be written as

$$\lambda_{f,s} = \frac{2}{L_x} \int_0^{L_x} \frac{b}{\Lambda} \, \mathrm{d}x = \frac{\sqrt{2}}{\pi L_x} \int_0^{L_x} \left(\frac{\mathrm{d}f}{\mathrm{d}y} \right)_{rms} \mathrm{d}x, \tag{4}$$

where the integral is evaluated in the cross-flow direction (see Appendix A). Here, we extend this idea to multiple length scales.

The function, $f(y)$, describes the elevation of the topography in the along-flow direction at any given x and can be written as a Fourier series,

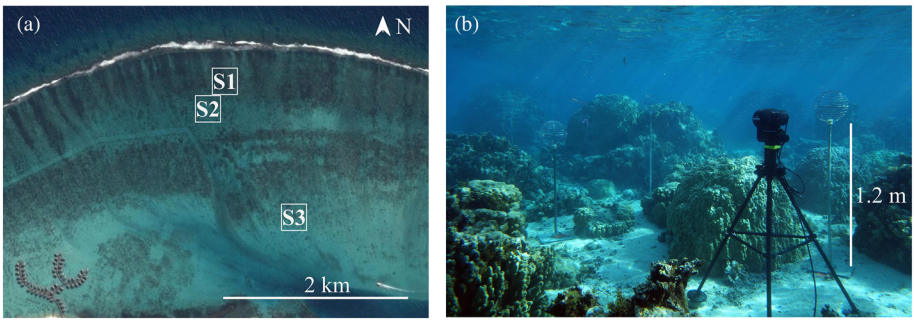

Figure 1. (a) Location of the three coral reef patches (10.24 m x 10.24 m) where the scanning sonar was deployed in the backreef of Moorea, French Polynesia (image from Google Earth CNES/Airbus, 2018). (b) Underwater photograph of Site 1 showing reef topography and the tripod-mounted 3-D multibeam scanning sonar. Wireframe spheres positioned at different heights above bottom are fixed location sonar targets used to register and merge multibeam scan data.

$$f(y) = \sum_{m=1}^{M} b_m \sin(k_m y + \phi_m). \tag{5}$$

We can then calculate $\lambda_{f,s}$ from Equation 3 as

$$\lambda_{f,s} = \frac{1}{L_y L_x} \int_0^{L_x} \int_0^{L_y} \left(\sum_{m=1}^{M} b_m k_m \cos(k_m y + \phi_m) \right)_{pos} \mathrm{d}y \mathrm{d}x, \tag{6}$$

where b_m, k_m, and ϕ_m are the amplitude, wavenumber, and phase of the m^{th} component. For a given surface the phasing of wavenumber components affects the total frontal area. If the various components are assumed to have random phasing, then both $f(y)$ and the slope, $\mathrm{d}f/\mathrm{d}y$, are approximately normally distributed. This assumption permits computation of $\lambda_{f,s}$ from the rms of the surface slope, which can be written in terms of the power spectrum, $P(k)$, such that

$$\lambda_{f,s} = \frac{1}{L_x\sqrt{2\pi}} \int_0^{L_x} \left(\frac{\mathrm{d}f}{\mathrm{d}y} \right)_{\mathrm{rms}} \mathrm{d}x = \frac{1}{L_x\sqrt{2\pi}} \int_0^{L_x} \left[\int_{k_{\min}}^{k_{\max}} k^2 P(k) \mathrm{d}k \right]^{1/2} \mathrm{d}x. \tag{7}$$

The derivation of Equation 7 is provided in Appendix A. Note that Equation 4 for a single sine wave and Equation 7 for a sum of random sine waves differ by a factor of $2/\sqrt{\pi} \approx 1.13$. However, the vertical distribution of frontal area is very different; it is close to Gaussian for a sum of sine waves with random phase but for a single sine wave has maxima at the peak and trough and a minimum at the mean elevation.

3. Methods

3.1. Field Data Collection

To test these ideas, high-resolution coral reef topography data were collected on a shallow coral reef flat, on the north shore of Moorea, French Polynesia (17°28.9′S; 149°50.3′W; Figure 1a). The backreef substrate is sand or flat pavement, populated by colonies of *Porites*, *Montipora*, and *Pocillopora* spp. that vary in size and spacing (Edmunds et al., 2010). Water depths in the backreef range from 1 to 4 m and corals typically occupy 30% to 90% of the water column (Hench & Rosman, 2013). For this study, three ~100m^2 backreef patches with contrasting coral topography characteristics were surveyed (Figure 1a). Site 1 (S1) was composed of mostly large, densely packed coral colonies, Site 2 (S2) was occupied by many smaller coral colonies, and Site 3 (S3) was more sparsely populated with a few large colonies.

High-resolution bathymetry data were collected using a three-dimensional scanning multibeam sonar (Teledyne BlueView, BV5000), which consists of a 2.25 MHz sonar head attached to a pan/tilt positioner (Remote Ocean Systems, P20; Figure 1b). The sonar and mechanical scanning system was deployed on a bottom-mounted tripod and cabled to a data acquisition system on a boat. The sonar head rotates 360° about a vertical axis and tilts at user-specified angles (e.g., 45° below horizontal) and was used to obtain circular

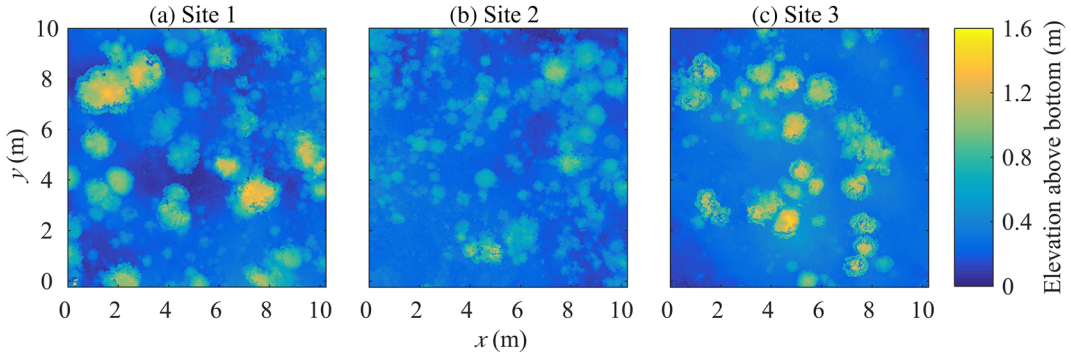

Figure 2. Topographic surfaces for each backreef site (a. Site 1, b. Site 2, and c. Site 3) derived from three-dimensional scanning multibeam sonar data.

swaths of topography 0.5 to 5 m away. To resolve the 3-D structure of the reef, multiple scans were taken at different angles and locations within each patch. Registration points were established from 8 to 12 diver-deployed targets at each site, which consisted of a metal wireframe sphere attached to a pole and a weighted PVC baseplate (Figure 1b). At Site 2, 9 scans of the bottom were taken, and 21 scans were taken at Sites 1 and 3 due to the higher relief at these sites that obstructed line-of-sight views of the multibeam sonar. Due to the variation in relief, the number of data points collected was not uniform across the patch, and some areas, such as between large coral colonies, were not well resolved. Individual sonar scans were merged together using registration points to create a single point cloud for each site using Leica Geosystems Cyclone software. Despite merging scans from many different angles some small gaps in the topography data remained due to occlusions in the sonar coverage; however, these gaps were minimal and not expected to significantly affect statistics calculated from the topography data. Erroneous points above the bottom (due to matter in the water column) and surface reflection artifacts were edited from point cloud data using CloudCompare software (CloudCompare, 2016). Point clouds were cropped to site boundaries, and mean elevation was computed from raw point cloud data for each 0.01 m × 0.01 m horizontal (x, y) cell within the 10.24 m × 10.24 m areas used in our analyses (Figure 2). Gridded elevation values were detrended by fitting a plane to the surface. Field tests prior to deployment suggest that accuracy of scans is on the order of 1 to 3 cm.

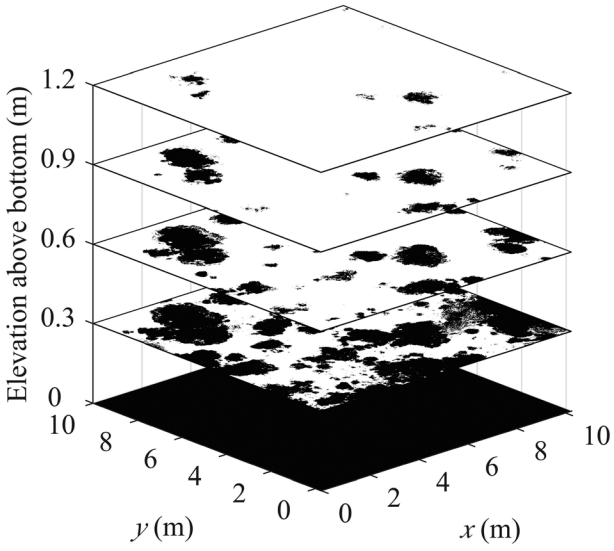

Figure 3. Selected binary x-y slices between the seafloor and top of the coral canopy indicating the presence (black) or absence (white) of substrate at backreef Site 1.

3.2. Topography as a Three-Dimensional Obstacle Array

To compute the geometric properties of three-dimensional roughness elements, 10.24 m × 10.24 m x-y slices were created at 0.02 m elevation intervals between the seafloor, defined as the lowest elevation at a site ($z = 0$), and top of the tallest coral (z_{max} = 1.51, 1.26, 1.51 m for Sites 1, 2, and 3, respectively; Figure 3). Each cell with an elevation value greater than or equal to the elevation of the slice was assigned a value of 1 (i.e., substrate cells); all other cells were assigned a value of 0 (i.e., fluid cells). For each resulting binary slice, connected substrate cells were assigned to the same group. This process for identifying individual roughness elements is valid for mounding corals, but would not capture the fluid space between branches for other types of corals. Roughness elements near the seafloor could not be differentiated from underlying substrate (see Figure 3), thus, the geometry of coral colonies was quantified using slices above 30% of the maximum topography elevation (z_{30} = 0.45, 0.38, and 0.45 m for Sites 1, 2, and 3, respectively).

For each numbered roughness element in an x-y slice, the maximum width in the cross-flow direction, $l_{x,i}$, was quantified as the side length in the x direction of the smallest rectangle enclosing the element in the x-y plane. The plan area of each element, $A_{p,i}$, was computed by multiplying the area of each cell (0.0001 m^2) by the total number of cells in a given

element at z_{30}. The height of each roughness element, $l_{z,i}$, was quantified using both the mean ($\bar{l}_{z,i}$) and maximum (max ($l_{z,i}$)) elevation of all cells belonging to an element. For each coral, we also computed the distances between all the boundary coordinates of the coral and all the boundary coordinates of all other corals within the patch. The shortest of these distances was used to represent the spacing (S_i) corresponding to that coral. The frontal area of an element, $A_{f,i}$, was computed as the sum of the frontal area in each slice between z_{30} and z_{max}. The volume of each element, V_i, was found by multiplying the volume of each cell (2×10^{-6} m^3) by the total number of cells belonging to an element between z_{30} and z_{max}.

3.3. Topography as a Two-Dimensional Continuous Surface

Topography was also analyzed as a two-dimensional elevation field $f(x, y)$. Computed properties of the elevation field were as follows: the distribution of elevation and its moments, the distribution and moments of along-flow slope ($\partial f/\partial y$), and variation of elevation with spatial scale.

Power spectral density, $P(k)$, of the elevation field was quantified at each site using one-dimensional spatial series in the y direction. Linear trends were removed from each spatial series prior to computing $P(k)$ using Welch's (1967) method. A single average spectrum for each patch was computed as the mean of the 1,024 one-dimensional spectra. The power spectrum decays with wavenumber according to the power law

$$P(k) = bk^{-\beta}. \tag{8}$$

The scaling exponent, β, was computed from a linear fit to the mean spectrum and provides a measure of the global scaling behavior of the elevation field at each site.

3.4. Idealized Fractional Brownian Surfaces

To quantify the effect of scaling behavior on the roughness statistics, we constructed idealized topographies using fractional Brownian processes. Fractional Brownian processes have been previously used as models for natural reefs (Purkis & Kohler, 2008; Zawada & Brock, 2009). Fractional Brownian topographies are Gaussian and monofractal with nonstationary covariance functions defined by a single scaling exponent, known as the Hurst exponent, H, (Hurst, 1951):

$$\mathrm{cov}(Z_s, Z_t) = s^{2H} + t^{2H} - s{-}t^{2H}. \tag{9}$$

H varies between 0 and 1 and controls the spatial autocorrelation of the elevation field. Z_s is the elevation series as a function of position index s along a surface. Z_t is the elevation as a function of independent position index t and is shifted from Z_s by s-t increments along the surface. When $0 < H < 0.5$, the increments of the surface are negatively correlated and exhibit small-scale spatial variations consistent with qualitatively rougher topography. When $0.5 < H < 1$, the increments of the surface are positively correlated and exhibit large-scale spatial variations consistent with qualitatively smoother surfaces. When $H = 0.5$ the increments are independent or uncorrelated (Kroese & Botev, 2015; Mandelbrot & van Ness, 1968). For fractional Brownian processes the relationship between H and β, the slope of the power spectrum, is $H = (\beta - 1)/2$. For monofractal processes such as fractional Brownian topography, a single scaling exponent describes the variation in elevation with scale everywhere along the surface.

For this study, a set of fifty surfaces were generated for each specified H value (0.3, 0.5, 0.7, 0.9; Figure 9) using the algorithm of Kroese and Botev (2015). Elevation values were normalized between −0.5 and 0.5. For a given fractional Brownian surface, elevation and bottom slope are normally distributed and the standard deviation of the elevation increases with H, whereas standard deviation of bottom slope decreases with H.

4. Results

4.1. Topography as a Three-Dimensional Obstacle Array

For roughness elements at three backreef study sites, the average height of each obstacle, $\bar{l}_{z,i}$, and the maximum height of each obstacle, max ($l_{z,i}$), are positively correlated with obstacle width, $l_{x,i}$ (Figure 4). Wider elements are taller but also less numerous, which is consistent with our qualitative observations from the field site (Figure 1) and studies on other reefs colonized by *Porites* (e.g., Boulay et al., 2012). The widest

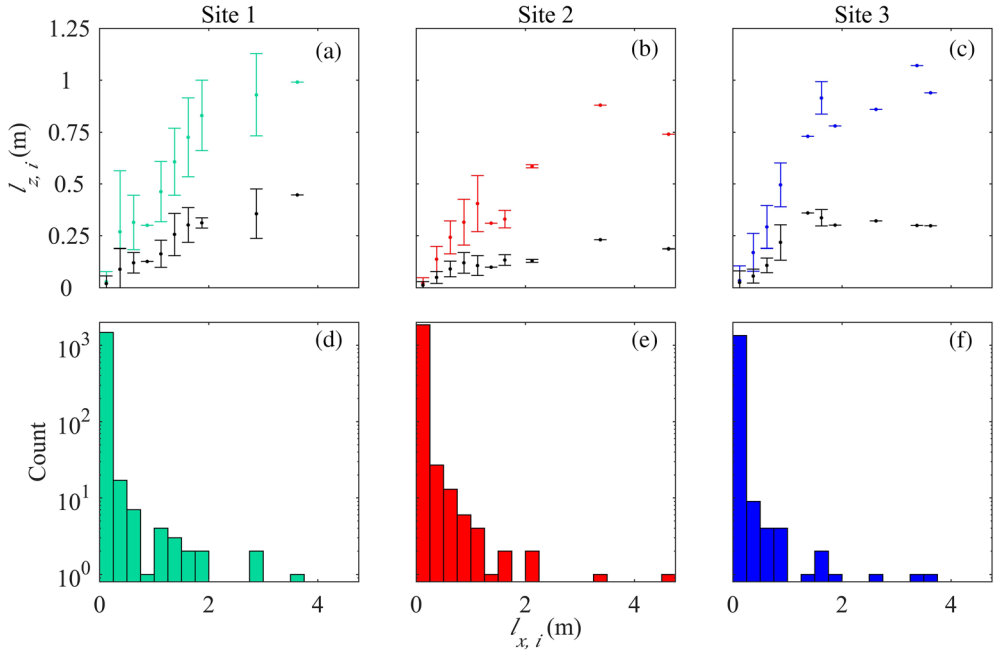

Figure 4. (a–c) Distribution of mean (black) and maximum (colored) coral height, $l_{z,i}$. Error bars indicate standard deviation of coral height. (d–f) Number of corals as a function of maximum width, $l_{x,i}$, in the cross-flow (x direction) at Sites 1, 2, and 3.

roughness elements ($l_{x,i}$ = 4.5 m) at Site 2 are aggregates of individual coral colonies. For a given $l_{x,i}$, roughness elements are generally shorter at Site 2 than at Sites 1 and 3; however, Site 2 has more elements than the other sites.

For all sites, roughness elements are approximately circular in the horizontal plane, as evident by the relationship between $l_{x,i}$ and $\sqrt{A_{p,i}}$, which is well represented by that for a circle (Figure 5a). However, $\bar{l}_{z,i}$ is generally less than the element's horizontal radius, $0.5l_{x,i}$ (Figure 5b). The best fit power law relationship between $\bar{l}_{z,i}$ and $l_{x,i}$ is $\bar{l}_{z,i} = 0.13l_{x,i}^{1.02}$. Therefore, elements in the backreef are better represented by semispheroid than by hemisphere geometry. There was no relationship between the horizontal length scale of roughness elements and the spacing between neighboring elements (Figure 5c). In general, the spacing was less than 1 m, and less than $l_{x,i}$.

The volume (V_i) and frontal area ($A_{f,i}$) of roughness elements also increased with $l_{x,i}$ (Figure 6). For an element with a given $l_{x,i}$, V_i is overestimated by cube, hemisphere, and cylinder geometries by up to 2 orders of

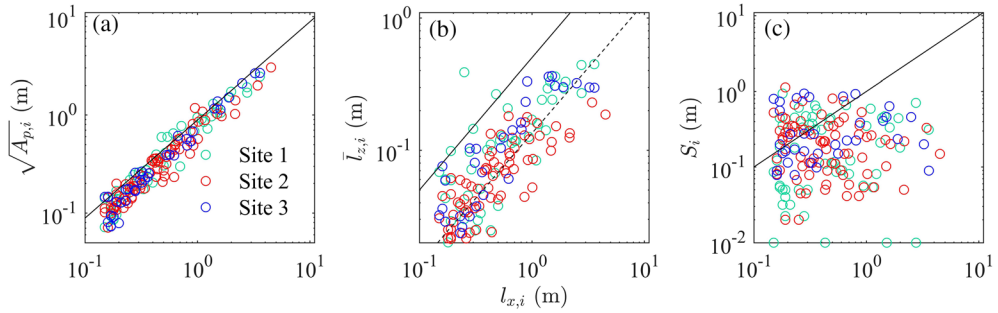

Figure 5. (a) Square root of the plan area, $\sqrt{A_{p,i}}$; (b) coral height, $\bar{l}_{z,i}$, quantified as the mean elevation of the top surface of an element; and (c) spacing, S_i, as a function of cross-flow width, $l_{x,i}$, for roughness elements greater than ≥0.15 m at the backreef sites. Solid line indicates expected relationship between properties for an array of hemispheres where $S_i = l_{x,i}$. For the three sites, $\bar{l}_{z,i} = 0.13l_{x,i}^{1.02}$ (dashed line) as determined from the average regression between $l_{x,i}$ and $\bar{l}_{z,i}$ for each site.

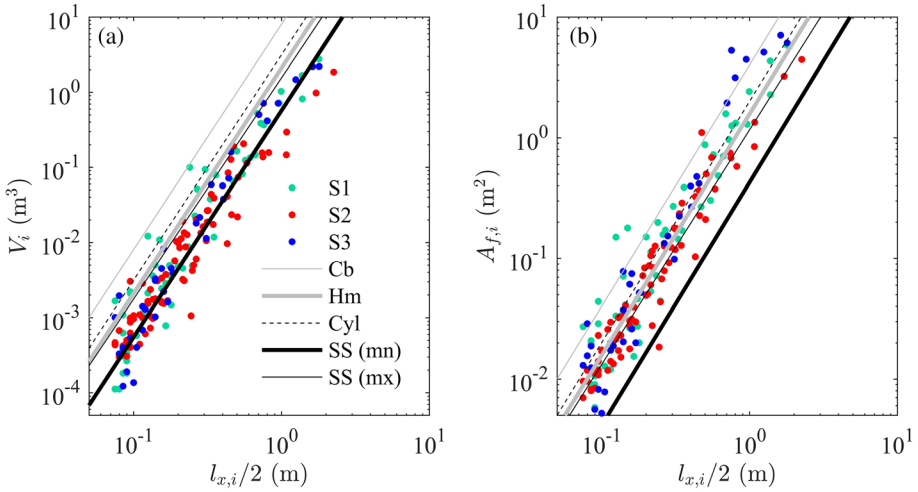

Figure 6. (a) Volume, V_i; and (b) frontal area, $A_{f,i}$, of corals at Sites 1, 2, and 3 (filled circles). Curves for cylinder (Cyl), cube (Cb), hemisphere (Hm), and semispheroid (SS) geometries are shown for comparison. For the idealized cylinder, $l_{z,i} = 0.5l_{x,i}$. For the idealized semispheroid, $\bar{l}_{z,i}=0.13l_{x,i}^{1.02}$ or $\max(l_{z,i})=0.38l_{x,i}^{0.94}$ as estimated from the mean or maximum elevation of each coral. Only elements with $l_{x,i} \geq 0.15$ m are shown for backreef sites.

magnitude (Figure 6a). The best estimate of V_i was achieved by assuming semispheroid geometry based on the empirical relationship between $l_{x,i}$ and $l_{z,i}$ quantified using the mean or maximum height of cells in the element. This roughly provides lower and upper bounds of element volume. $A_{f,i}$ computed using the obstacle approach is best approximated by semispheroid geometry based on $l_{x,i}$ and max ($l_{z,i}$) (Figure 6b). This was used as a model for the topography in further analyses.

4.2. Topography as a Two-Dimensional Continuous Surface

For backreef topography, the elevation field is non-Gaussian (Figures 7a–7c). The distributions of elevation exhibit positive skewness due to the presence of coral colonies on the relatively flat substrate. Larger coral

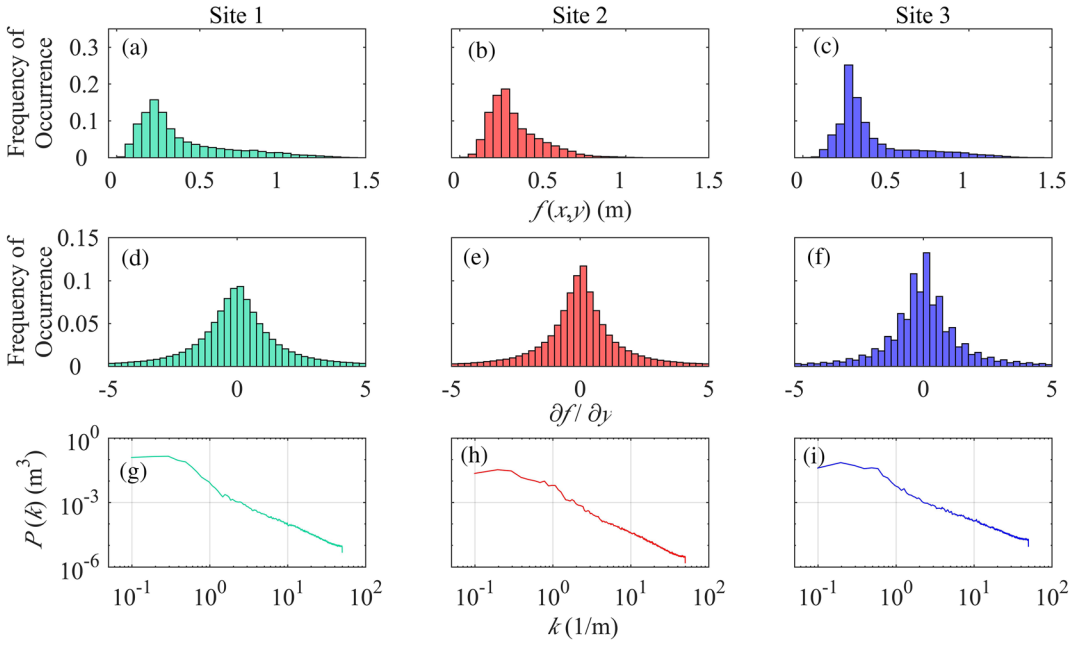

Figure 7. (a–c) Distributions of bottom elevation, $f(x, y)$; (d–f) distributions of along-flow bottom slope, $\partial f/dy$; and (g–i) average spectrum of elevation in the along-flow direction, $P(k)$, at Sites 1, 2, and 3.

Table 1
Roughness Density, λ_f, for Obstacle and Surface-Based Estimates and Models for the Three Backreef Sites

	Backreef sites			Fractional Brownian fields			
	Site 1	Site 2	Site 3	$H = 0.3$	$H = 0.5$	$H = 0.7$	$H = 0.9$
Obstacle $\lambda_{f,o}$	0.45	0.34	0.51	0.53 ± 0.1	0.19 ± 0.04	0.07 ± 0.03	0.03 ± 0.02
Semi-spheroid model (Equation 2)	0.47	0.39	0.31				
Surface $\lambda_{f,s}$ (Equation 3)	1.03	0.77	1.17	1.27 ± 0.23	0.51 ± 0.10	0.19 ± 0.07	0.07 ± 0.04
Random sine model							
df/dy (Equation 7)	1.67	1.13	2.09	1.27 ± 0.23	0.51 ± 0.10	0.19 ± 0.07	0.07 ± 0.03
$P(k)$ (Equation 7)	1.96	1.19	2.41	1.56 ± 0.28	0.60 ± 0.12	0.21 ± 0.08	0.08 ± 0.03
Single sine model							
df/dy (Equation 4)	1.88	1.27	2.35	1.44 ± 0.26	0.57 ± 0.11	0.21 ± 0.08	0.08 ± 0.03

Note. For fractional Brownian topography, values show the mean and standard deviation of λ_f for 50 surfaces for each H value.

colonies at Sites 1 and 3 result in greater standard deviation ($\sigma = 0.27$, 0.24 m) and skewness ($Skew = 1.33$, 1.62) relative to Site 2 ($\sigma = 0.16$ m; $Skew = 1.24$). The mode of the elevation corresponds to the seafloor, which is more pronounced at Site 3 because the seafloor is flat and sandy with fewer coral fragments and colonies.

The distribution of the bottom slope is symmetric, with zero mean and zero skewness (Figures 7d–7f), but differs from a Gaussian distribution. The standard deviation of the bottom slope is greatest at Sites 1 and 3 ($\sigma = 4.32$, 5.84) and lowest at Site 2 ($\sigma = 2.90$).

Across the entire wavenumber range, mean spectral density is greater at Sites 1 and 3 relative to Site 2 owing to greater variance in elevation at those sites (Figures 7g–7i). Spectral slope is similar across the three sites, and $\beta = 1.68$, 1.78, and 1.44, at Sites 1, 2, and 3, respectively. This corresponds to global scaling exponents $H = 0.34$, 0.39, and 0.22. The three sites exhibit isotropy in global scaling, as H is similar in both cross- and along-flow directions.

4.3. Roughness Density

We estimated roughness density, λ_f, from the reef topography data and idealized fractional Brownian surface data using obstacle- and surface-based approaches. Estimates were then compared with analytical expressions derived for several different model surfaces (Table 1).

4.3.1. Obstacle-Based Estimates and Model

To estimate $\lambda_{f,o}$, we summed the frontal areas in each x-y slice between the seafloor and top of the tallest coral. For the three reef sites, this gave similar estimates of $\lambda_{f,o}$ (0.45, 0.34, and 0.51; Table 1). Corals in the backreef have similar morphologies; thus, $\lambda_{f,o}$ depends on both the size and number of elements present. Roughness elements at Site 3 are larger and less numerous, while there are a greater number of smaller elements at Site 2.

We find that fractional Brownian topographies defined by similar values of H as the reef topographies ($H \sim 0.3$) have similar $\lambda_{f,o}$, despite differences in the geometry, number, and size of elements between the natural reef and Brownian surfaces (Table 1). Roughness density is highest for topographies defined by a small H value, which are characterized by a large number of very small roughness elements due to the negative covariance of the surface. As H increases, the frontal area of individual roughness elements increases while the number of elements decreases, but the net result is lower $\lambda_{f,o}$, as computed using the obstacle-based estimation method.

We compared $\lambda_{f,o}$ estimates for backreef topography with those for arrays of semispheroids (Table 1; Figure 8a). For the semispheroid model (where $\alpha = \pi/4$ in Equation 2), the relationship between $l_{x,i}$ and max ($l_{z,i}$) at z_{30} was used to predict $l_{x,i}$ at the seafloor, which allowed us to estimate $\lambda_{f,o}$ over the entire height of the canopy. The frontal area per unit volume, $a = \Delta A_f / A_T \Delta z$, where ΔA_f is the frontal area in a given slice and Δz is the height of the slice, decreases from a maximum at the seafloor to a minimum at

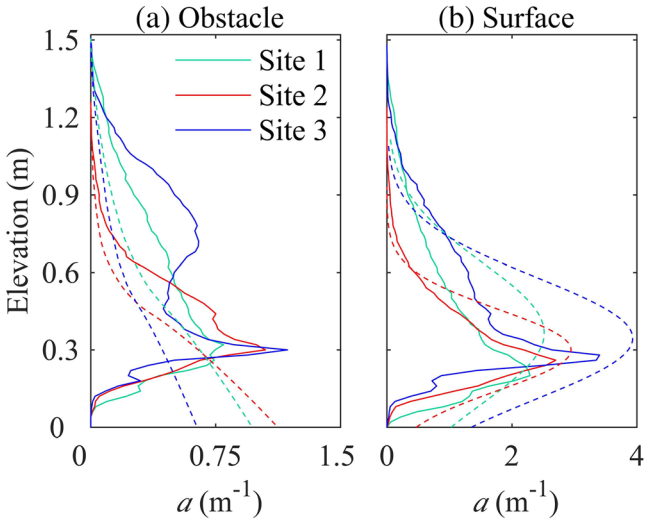

Figure 8. Frontal area per unit volume, a, as a function of height above bottom for (a) actual obstacle (solid lines) and modeled obstacle (i.e., semispheroid; dashed lines); and (b) surface approaches using actual bottom slope (solid lines) and PDF of bottom slope (dashed lines) for backreef sites.

the top of the canopy for the semispheroid model (Figure 8a). The a based on actual reef geometry increases from the seafloor to a peak at approximately 0.30 m above the bottom. Near the seafloor, aggregates of coral colonies merge into a single obstacle representing solid substrate, so a decreases and ultimately goes to zero at the lowest substrate elevation in the patch. At Sites 1 and 2, $\lambda_{f,o}$ based on the semispheroid model agrees well with estimates based on reef topography measurements, despite differences in profile shapes (Table 1). At Site 3, there was a second peak in a at 0.7 m above bottom due to the separation of elements that are connected closer to the seafloor. This contributes frontal area that is not captured by the semispheroid model and causes the model to under predict $\lambda_{f,o}$ at Site 3 (Table 1). For the fractional Brownian topographies, a is normally distributed as a function of height above bottom (Figure 10a).

4.3.2. Surface-Based Estimates and Models

The slope of the topography was used to estimate $\lambda_{f,s}$ (Equation 3). For the reef sites, Site 3 had the largest $\lambda_{f,s}$ and Site 2 had the smallest ($\lambda_{f,s} = 1.03$, 0.77, 1.17; Table 1). Although the relative magnitudes of $\lambda_{f,s}$ had a similar pattern among reef patches to that for $\lambda_{f,o}$, values from the surface approach were consistently about a factor of 2 larger than estimates from the obstacle approach (Table 1). The surface-based estimates had a similar distribution of a as a function of height above bottom, where peak a occurred ~0.3 m above the seafloor (Figure 8b).

We compared estimates of $\lambda_{f,s}$ with those for a model surface composed of a sum of sine waves with varying wavenumbers, amplitudes determined from the power spectrum of measured topography, and random phase (Equation 5). Roughness densities computed from $(df/dy)_{rms}$ using the theoretical expression for a sum of random sinusoids (Equation 6; $\lambda_f = 1.67$, 1.13, and 2.09) were about 70% larger than actual $\lambda_{f,s}$. This overestimation is attributable to the phasing of the different wavenumber components of the signal, which affects the total frontal area of the surface. If different wavenumber components have random phasing, both elevation and slope are normally distributed. For the backreef topography, elevation and slope are not normally distributed (Figures 7a–7f), resulting in a poor approximation.

For fractional Brownian topographies, actual $\lambda_{f,s}$ agreed closely with the expression for random sinusoids when computed using $(df/dy)_{rms}$ (Table 1 and Figure 10b). Estimates based on $P(k)$ slightly overestimated $\lambda_{f,s}$. For $\beta < 2$, the integral of $P(k)$ tends to infinity as k_{max} approaches infinity, meaning that small fluctuations contribute substantially to the total frontal area. For this reason, the agreement between estimates is worse at smaller values of H.

Representing the surface as a single sine wave, as proposed by Rogers et al. (2018), results in poorer agreement with surface slope estimates for both reef and fractional Brownian topographies (Table 1). Estimates of $\lambda_{f,s}$ based on the single sine wave model are a factor of 1.13 higher than estimates based on the random sine wave model.

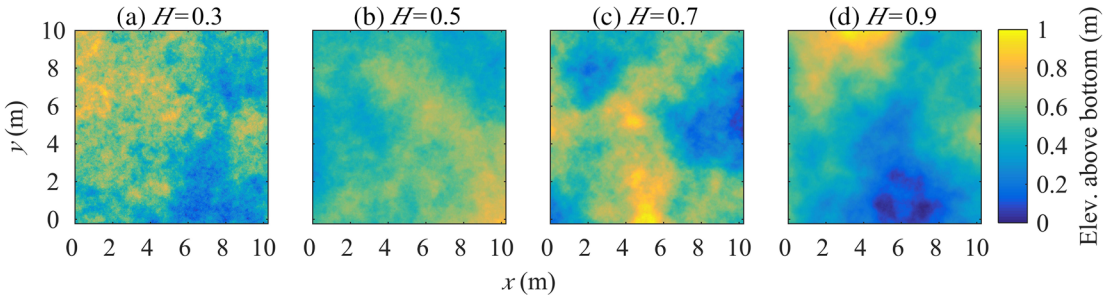

Figure 9. Example topographic surfaces derived from fractional Brownian motion with different values of H: (a) $H = 0.3$, (b) $H = 0.5$, (c) $H = 0.7$, and (d) $H = 0.9$.

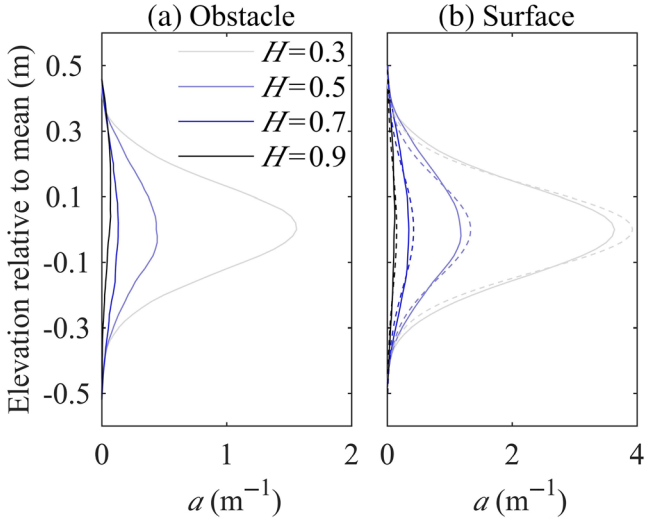

Figure 10. Mean a as a function of elevation relative to the mean for (a) actual obstacle (solid lines); and (b) actual bottom slope (solid lines) and PDF of bottom slope (dashed line) approaches for topographic surfaces derived from fractional Brownian motion.

5. Discussion

5.1. Obstacle Versus Surface-Based Estimates of Roughness Density

We have illustrated that λ_f can be computed for natural multiscale topography data using obstacle and surface-based approaches. However, for our reef data set, surface-based estimates were a factor of 2 higher than obstacle-based estimates. The two approaches for computing roughness density did not agree because small-scale roughness on the surface of coral colonies is captured by the surface approach, but is not captured by the obstacle approach. This occurs due to the way binary cells are grouped and assigned to an object within x-y slices (Figures 11a and 11c). For substrate cells that are connected in the x-y plane (i.e., belong to the same colony group) and occupy the same cross-flow (x) position, the obstacle estimate only accounts for the frontal area of one cell, whereas the surface estimate accounts for all vertical rises that face the flow. For the example transect shown in Figure 11c, the frontal area estimated by the obstacle approach is 0.0002 m^2, but is 0.001 m^2 for the surface approach, a difference of a factor of 5. For the smoothed roughness element in Figure 11b, obstacle and surface estimates of frontal area are equivalent.

When natural reef topography is represented as a continuous surface, information about the complete range of length scales is retained. The λ_f can then be estimated from the pointwise slope in the along-flow direction (Equation 3). Accounting for all roughness length scales may be important for estimating the drag exerted on the flow.

5.2. Effect of Smoothing on Estimates Roughness Density

Given the substantial contribution of high wavenumber components to total A_f, it is important to consider relevant length scales together with data accuracy and resolution prior to smoothing or filtering elevation

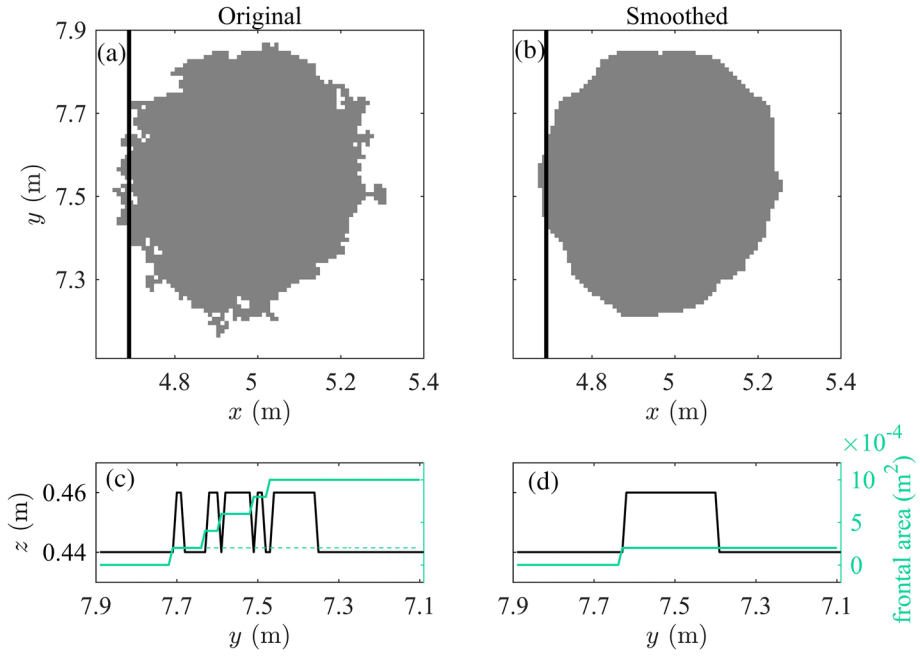

Figure 11. (a) Plan area view of an example single obstacle at z_{30}. Black line shows location of along-flow transect shown in (c). Frontal areas of the transect (cross-flow width = 0.01 m) estimated by obstacle and surface approaches are 0.0002 m^2 (dashed) and 0.001 m^2 (solid), respectively. (b) The same obstacle when elevation data have been smoothed using a window size l_{win} = 8 cm, and along-flow transect shown in (d). Frontal area of the transect is 0.0002 m^2 for both obstacle and surface approaches.

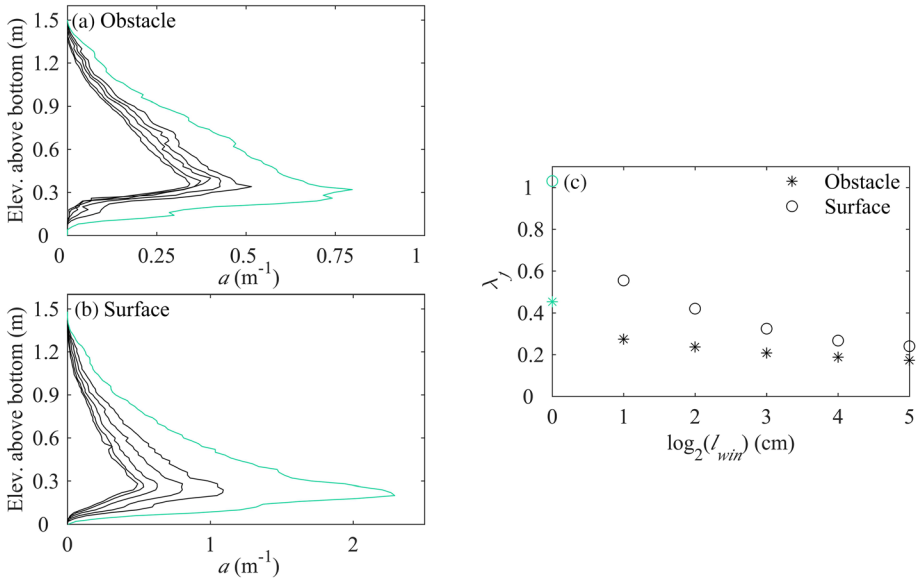

Figure 12. The effect of smoothing on a at Site 1 for (a) obstacle and (b) surface approaches as a function of elevation above bottom. Smoothing was performed for various window sizes with side length $l_{win} = 2^n$, where $1 \leq n \leq 5$. (c) λ_f as a function of l_{win} for the entire canopy. Values with no smoothing are shown in green (see Table 1 and Figure 8).

data. Both obstacle and surface-based λ_f estimates decrease with increased filter window size, l_{win} (Figure 12). Furthermore, as l_{win} increases, obstacle-and surface-based estimates of λ_f converge, as do estimates computed from $P(k)$ and $(df/dy)_{rms}$ for the sinusoidal surface models. It is therefore important to consider the effects of smoothing when interpreting reported λ_f values. For example, for $l_{win} \geq 0.08$ m, λ_f is approximately 0.2 to 0.3 for obstacle- and surface-based estimates. These values are similar to values reported in Rogers et al. (2018) for reef topography that had been smoothed to 0.10 to 0.30 m resolution. From these values, Rogers et al. (2018) inferred a low concentration of roughness elements. However, the hydrodynamic roughness, z_0, was underestimated, and an additional roughness term was needed to capture the contribution of smaller, unresolved scales. Without smoothing, when all length-scales are taken into account, $\lambda_{f,s}$ is close to 1 for our reef data set. However, it is important to not only consider total A_f, but the contribution of various wavenumber components to A_f as drag on the flow may be length-scale dependent.

5.3. Models for Natural Reef Topography

Roughness densities estimated by modeling the topography as an array of semispheroids agree relatively well with obstacle-based estimates because most of the colonies have quasi-uniform, semispheroid morphology that is characteristic of mounding corals. The semispheroid model does not capture the contribution of small-scale (<0.15 m) fluctuations to total A_f, which should lead to an underestimation of $\lambda_{f,o}$. However, the semispheroid model overestimates the frontal area near the seafloor, and these two sources of error partially cancel, resulting in better than expected agreement between the model and actual $\lambda_{f,o}$ (Figure 8a).

If topography is conceptualized as a two-dimensional surface, our results show that models that assume random phasing of wavenumber components do not give good estimates of $\lambda_{f,s}$ for reef topography similar to our reef sites. This is because, unlike fractional Brownian topography and some natural topographies like gravel beds (Stubbs et al., 2018), $f(x, y)$ and $\partial f/\partial y$ do not have Gaussian distributions. Therefore, the assumption of randomly phased wavenumber components results in overestimates of $\lambda_{f,s}$.

Similarly, estimates of $\lambda_{f,s}$ based on $P(k)$ assume that the decay in variance as a function of wavenumber is the same everywhere along the surface (i.e., homogenous). While this assumption is valid for monofractal processes like fractional Brownian topography, the presence of multiple scaling behaviors is ubiquitous across various forms of natural topography (Duvall et al., 2019; Lavallée et al., 1993; Tchiguirinskaia et al., 2000; Weissel et al., 1994; Wendt et al., 2009). In our previous work, we found that coral reef topography was multifractal across scales of 4–32 m (Duvall et al., 2019). Similar analysis of the reef patch topography data used in this study showed that it was multifractal across scales of 0.02–1.28 m (see

supporting information). The multifractality of coral topography at colony and reef scales (Duvall et al., 2019) suggests a need for more complex models. However, it is difficult to find models for natural topography that are both multifractal and non-Gaussian (Chainais, 2007). Future work should explore multifractal models, like multiplicative cascades, that have distributions (e.g., log-normal) more similar to natural reef data, or, more straightforwardly, compute frontal area directly from high-resolution topographic measurements.

6. Conclusions

At present, in studies of flow over terrestrial and shallow-water boundaries, topography is represented either as an array of three-dimensional obstacles or as a two-dimensional surface of elevation. Here, we present the first attempt to reconcile obstacle and surface representations of multiscale topography by comparing roughness density calculations based on both approaches. Our roughness density estimates for natural coral reef topography based on obstacle geometry and surface slope do not agree. The discrepancy between estimates is due to high wavenumber surface roughness that is captured by the surface slope approach but is not captured by the obstacle geometry approach. Simple surface models for topography should be used with caution, however, because as shown here natural topography may not obey assumptions of Gaussian distribution and homogeneous scaling. Furthermore, analyses presented in this paper are only appropriate for topography that can be represented as a single elevation value for each horizontal position. More work is needed on how to best represent reefs with branching morphologies.

As small length scales can contribute substantially to total frontal area, it is important to consider data quality and filter the data in a way that removes noise but still captures real, small-scale variability. Because small-scale features may interact with flow in a different way to larger-scale features, drag may be length-scale dependent. It is therefore important to consider not only the total frontal area of the surface, but also the distribution of frontal area across length scales.

Appendix A: Estimating Frontal Area From Surface Models for Topography

Here we provide derivations of expressions for frontal area per unit plan area for two idealized topographies that have been used as models for coral reefs and other multiscale topography: a single sinusoid and a sum of many sinusoids with different wavenumbers.

Single Sine Wave Model for Topography

We first consider a surface modeled by a single equivalent sine wave, as proposed by Rogers et al. (2018),

$$f(y) = b\sin(ky), \tag{A1}$$

where b is the amplitude and k is the wavenumber, such that $k = 2\pi/\mathrm{L}$. The frontal area per unit plan area for this surface is

$$\lambda_{f,s} = \frac{A_f}{A_T} = \frac{bk}{\pi} \tag{A2}$$

The slope of the surface is

$$\frac{\mathrm{d}f}{\mathrm{d}y} = b\ k\cos(k\ y). \tag{A3}$$

The rms of a sinusoid is the amplitude divided by $\sqrt{2}$; therefore,

$$\left(\frac{\mathrm{d}f}{\mathrm{d}y}\right)_{rms} = \frac{1}{\sqrt{2}} b\ k. \tag{A4}$$

The roughness density can therefore be written as

$$\lambda_{f,s} = \frac{\sqrt{2}}{\pi}\left(\frac{\mathrm{d}f}{\mathrm{d}y}\right)_{rms} \tag{A5}$$

Integrating in the cross-flow direction to compute $\lambda_{f,s}$ for a 2-dimensional surface yields Equation 4,

$$\lambda_{f,s} = \frac{\sqrt{2}}{\pi L_x} \int_0^{L_x} \left(\frac{\mathrm{d}f}{\mathrm{d}y}\right)_{rms} \mathrm{d}x \tag{A6}$$

Multisine Wave Model for Topography

We now consider a multiscale surface represented as a sum of sinusoids,

$$f(y) = \sum_{m=1}^{M} b_m \sin(k_m y + \phi_m). \tag{A7}$$

The slope in the along-flow direction is

$$\frac{\mathrm{d}f}{\mathrm{d}y} = f'(y) = \sum_{m=1}^{M} b_m k_m \cos(k_m y + \phi_m) \tag{A8}$$

If we assume that the different wavenumber components have random phasing, the frequency distributions of both $f(y)$ and $\mathrm{d}f/\mathrm{d}y$ are approximately Gaussian, such that

$$p(f) = \frac{1}{\sqrt{2\pi m_0}} \exp\left[-\frac{1}{2}\left(\frac{f^2}{m_0}\right)\right]. \tag{A9}$$

$$p(f') = \frac{1}{\sqrt{2\pi m_2}} \exp\left[-\frac{1}{2}\left(\frac{f'^2}{m_2}\right)\right] \tag{A10}$$

where,

$$m_0 = \sum_{m=1}^{M} \frac{1}{2} b_m^2 = \sigma^2. \tag{A11}$$

$$m_2 = \sum_{m=1}^{M} \frac{1}{2} b_m^2 k_m^2 = \left(\frac{\mathrm{d}f}{\mathrm{d}y}\right)_{rms}^2. \tag{A12}$$

In the limit of closely spaced wavenumber components, $b_m = (2P(k_m)\mathrm{d}k)^{1/2}$, where $P(k)$ is the power spectral density at wavenumber k, and m_0 and m_2 can be written as functions of $P(k)$

$$m_0 = \int_{k_{\min}}^{k_{\max}} P(k)\mathrm{d}k = \sigma^2 \tag{A13}$$

$$m_2 = \int_{k_{\min}}^{k_{\max}} k^2 P(k)\mathrm{d}k = \left(\frac{\mathrm{d}f}{\mathrm{d}y}\right)_{rms}^2. \tag{A14}$$

From Equation 3,

$$\lambda_{f,s}\big|_x = \frac{1}{L_y}\int_0^{L_y}\left(\frac{\mathrm{d}f}{\mathrm{d}y}\right)_{\mathrm{pos}} \mathrm{d}y = \int_0^{\infty} f' p(f')\ \mathrm{d}f' = \int_0^{\infty} f' \frac{1}{\sqrt{2\pi m_2}} \exp\left[\frac{-f'^2}{2m_2}\right] \mathrm{d}f' \tag{A15}$$

Using the variable substitution $g = f'/\sqrt{m_2}$,

$$\lambda_{f,s}\big|_x = \sqrt{\frac{m_2}{2\pi}} \int_0^{\infty} g \exp\left[-\frac{g^2}{2}\right] \mathrm{d}y = \sqrt{\frac{m_2}{2\pi}}. \tag{A16}$$

Integrating over the cross-flow direction yields Equation 7,

$$\lambda_{f,s} = \frac{1}{L_x\sqrt{2\pi}} \int_0^{L_x} \left(\frac{\mathrm{d}f}{\mathrm{d}y}\right)_{rms} \mathrm{d}x = \frac{1}{L_x\sqrt{2\pi}} \int_0^{L_x} \left[\int_{k_{\min}}^{k_{\max}} k^2 P(k)\mathrm{d}k\right]^{1/2} \mathrm{d}x. \tag{A17}$$

Data Availability Statement

Data in this work are archived and available in the NSF LTER data repository (https://doi.org/10.6073/pasta/4af096f1d8b601e56f338b04f1bca58e).

Acknowledgments
Support for this work came from the National Science Foundation Physical Oceanography program (OCE-1435530 and OCE-1435133). The Moorea Coral Reef LTER program (OCE-1637396) provided logistical and field support for the reef topography measurements. M. Duvall gratefully acknowledges fellowship support from the Duke University Graduate School. This research was conducted under permits issued by the French Polynesian Government (Délégation à la Recherche) and the Haut-commissariat de la République en Polynésie Francaise.

References

Asher, S., Niewerth, S., Koll, K., & Shavit, U. (2016). Vertical variations of coral reef drag forces. *Journal of Geophysical Research: Oceans*, *121*, 3549–3563. https://doi.org/10.1002/2015JC011428

Boulay, J. N., Cortés, J., Nivia-Ruiz, J., & Baums, I. B. (2012). High genotypic diversity of the reef-building coral *Porites lobata* (Scleractinia: Poritidae) in Isla del coco National Park, Costa Rica. *Revista de Biología Tropical*, *60*, 279–292.

Chainais, P. (2007). Infinitely divisible cascades to model the statistics of natural images. *IEEE Transactions on Pattern Analysis and Machine Intelligence*, *29*(12), 1–15.

CloudCompare (version 2.7) [GPL software]. (2016). Retrieved from http://www.cloudcompare.org/

Coceal, O., & Belcher, S. E. (2004). A canopy model of mean winds through urban areas. *Quarterly Journal of the Royal Meteorological Society*, *130*(599), 1349–1372. https://doi.org/10.1256/qj.03.40

Di Sabatino, S., Solazzo, E., Paradisi, P., & Britter, R. (2008). A simple model for spatially-averaged wind profiles within and above an urban canopy. *Boundary-Layer Meteorology*, *127*(1), 131–151. https://doi.org/10.1007/s10546-007-9250-1

Duvall, M. S., Hench, J. L., & Rosman, J. H. (2019). Collapsing complexity: Quantifying multiscale properties of reef topography. *Journal of Geophysical Research: Oceans*, *124*, 5021–5038. https://doi.org/10.1029/2018JC014859

Edmunds, P. J., Leichter, J. J., & Adjeroud, M. (2010). Landscape-scale variation in coral recruitment in Moorea, French Polynesia. *Marine Ecology Progress Series*, *414*, 75–89. https://doi.org/10.3354/meps08728

Finnigan, J. (2000). Turbulence in plant canopies. *Annual Review of Fluid Mechanics*, *32*(1), 519–571. https://doi.org/10.1146/annurev.fluid.32.1.519

Google Earth CNES/Airbus (2018). [*north shore of Moorea, French Polynesia*]. Retrieved from, https://www.google.com/earth

Grinvald, D. I., & Nikora, V. (1988). *Rechnaya turbulentsiya* [River turbulence]. Leningrad: Hydrometeo-Izdat.

Hench, J. L., & Rosman, J. H. (2013). Observations of spatial flow patterns at the coral colony scale on a shallow reef flat. *Journal of Geophysical Research: Oceans*, *118*, 1142–1156. https://doi.org/10.1002/jgrc.20105

Hurst, H. E. (1951). Long-term storage capacity of reservoirs. *Transactions of the American Society of Civil Engineers*, *116*, 770–808.

Kean, J. W., & Smith, J. D. (2006a). Form drag in rivers due to small-scale natural topographic features: 1. Regular sequences. *Journal of Geophysical Research*, *111*, F04009. https://doi.org/10.1029/2006JF000467

Kean, J. W., & Smith, J. D. (2006b). Form drag in rivers due to small-scale natural topographic features: 2. Irregular sequences. *Journal of Geophysical Research*, *111*, F04010. https://doi.org/10.1029/2006JF000490

Kroese, D. P., & Botev, Z. I. (2015). Spatial process simulation. In V. Schmidt (Ed.), *Stochastic geometry, spatial statistics, and random fields*, (pp. 369–404). Cham: Springer. https://doi.org/10.1007/978-3-319-10064-7_12

Kutzbach, J. (1961). Investigations of the modification of wind profiles by artificially controlled surface roughness. Studies of the three dimensional structure of the planetary boundary layer, Annual Report 1963, Department of Meteorology, University of Wisconsin, Madison, pp. 37–96

Lavallée, D., Lovejoy, S., Schertzer, D., & Ladoy, P. (1993). Nonlinear variability and landscape topography: Analysis and simulation. In L. De Cola, & N. Lam (Eds.), *Fractals in Geography*, (pp. 171–205). Englewood, New Jersey: Prentice-Hall.

Lentz, S. J., Churchill, J. H., & Davis, K. A. (2018). Coral reef drag coefficients—Surface gravity wave enhancement. *Journal of Physical Oceanography*, *48*(7), 1555–1566. https://doi.org/10.1175/JPO-D-17-0231.1

Lentz, S. J., Davis, K. A., Churchill, J. H., & DeCarlo, T. M. (2017). Coral reef drag coefficients – Water depth dependence. *Journal of Physical Oceanography*, *47*(5), 1061–1075. https://doi.org/10.1175/JPO-D-16-0248.1

Lettau, H. H. (1967). Problems of micrometeorological measurements. In E. F. Bradley, & O. T. Denmead (Eds.), *The collection and processing of field data*, (pp. 3–40). New York, NY: Interscience.

Lettau, H. H. (1969). Note on aerodynamic roughness-parameter estimation on the basis of roughness-element description. *Journal of Applied Meteorology*, *8*(5), 828–832. https://doi.org/10.1175/1520-0450(1969)008<0828:NOARPE>2.0.CO;2

Lowe, R. J., Falter, J. L., Bandet, M. D., Pawlak, G., Atkinson, M. J., Monismith, S. G., & Koseff, J. R. (2005). Spectral wave dissipation over a barrier reef. *Journal of Geophysical Research*, *110*, C04001. https://doi.org/10.1029/2004JC002711

Lowe, R. J., Falter, J. L., Koseff, J. R., Monismith, S. G., & Atkinson, M. J. (2007). Spectral wave flow attenuation within submerged canopies: Implications for wave energy dissipation. *Journal of Geophysical Research*, *112*, C05018. https://doi.org/10.1029/2006JC003605

Lowe, R. J., Koseff, J. R., & Monismith, S. G. (2005). Oscillatory flow through submerged canopies: 1. Velocity structure. *Journal of Geophysical Research*, *110*, C10016. https://doi.org/10.1029/2004JC002788

MacDonald, R. W., Griffiths, R. F., & Hall, D. J. (1998). An improved method for the estimation of surface roughness of obstacle arrays. *Atmospheric Environment*, *32*(11), 1857–1864. https://doi.org/10.1016/S1352-2310(97)00403-2

Mandelbrot, B. B., & van Ness, J. W. (1968). Fractional Brownian motions, fractional noises and applications. *SIAM Review*, *10*(4), 422–437. https://doi.org/10.1137/1010093

McDonald, C. B., Koseff, J. R., & Monismith, S. G. (2006). Effects of the depth to coral height ratio on drag coefficients for unidirectional flow over coral. *Limnology and Oceanography*, *51*(3), 1294–1301. https://doi.org/10.4319/lo.2006.51.3.1294

Monismith, S. G. (2007). Hydrodynamics of coral reefs. *Annual Review of Fluid Mechanics*, *39*(1), 37–55. https://doi.org/10.1146/annurev.fluid.38.050304.092125

Napoli, E., Armenio, V., & De Marchis, M. (2008). The effect of the slope of irregularly distributed roughness elements on turbulent wall-bounded flows. *Journal of Fluid Mechanics*, *613*, 385–394. https://doi.org/10.1017/S0022112008003571

Nepf, H. M. (1999). Drag, turbulence, and diffusion in flow through emergent vegetation. *Water Resources Research*, *35*(2), 479–489. https://doi.org/10.1029/1998WR900069

Nepf, H. M., & Vivoni, E. R. (2000). Flow structure in depth-limited, vegetated flow. *Journal of Geophysical Research*, *105*(C12), 28,547–28,557. https://doi.org/10.1029/2000JC900145

Nunes, V., & Pawlak, G. (2008). Observations of bed roughness of a coral reef. *Journal of Coastal Research*, *2*(2B), 39–50. https://doi.org/10.2112/05-0616.1

Purkis, S. J., & Kohler, K. E. (2008). The role of topography in promoting fractal patchiness in a carbonate shelf landscape. *Coral Reefs*, *27*(4), 977–989. https://doi.org/10.1007/s00338-008-0404-5

Raupach, M. R., & Thom, A. S. (1981). Turbulence in and above plant canopies. *Annual Review of Fluid Mechanics*, *13*(1), 97–129. https://doi.org/10.1146/annurev.fl.13.010181.000525

Reidenbach, M. A., Monismith, S. G., Koseff, J. R., Yahel, G., & Genin, A. (2006). Boundary layer turbulence and flow structure over a fringing coral reef. *Limnology and Oceanography*, *51*(5), 1956–1968. https://doi.org/10.4319/lo.2006.51.5.1956

Rogers, J. S., Maticka, S. A., Chirayath, V., Woodson, C. B., Alonso, J. J., & Monismith, S. G. (2018). Connecting flow over complex terrain to hydrodynamic roughness on a coral reef. *Journal of Physical Oceanography*, *48*(7), 1567–1587. https://doi.org/10.1175/JPO-D-18-0013.1

Samuel, L. C., & Monismith, S. G. (2013). Drag coefficients for single coral colonies and related spherical objects. *Limnology and Oceanography Fluids and Environments*, *3*(1), 173–181. https://doi.org/10.1215/21573689-2378401

Stewart, M. T., Cameron, S. M., Nikora, V. I., Zampiron, A., & Marusic, I. (2019). Hydraulic resistance in open-channel flows over self-affine rough beds. *Journal of Hydraulic Research*, *57*(2), 183–196. https://doi.org/10.1080/00221686.2018.1473296

Stubbs, A., Stoesser, T., & Bockelmann-Evans, B. (2018). Developing an approximation of natural, rough gravel riverbed both physically and numerically. *Geosciences*, *8*(12), 449–463. https://doi.org/10.3390/geosciences8120449

Tchiguirinskaia, I., Lu, S., Molz, F. J., Williams, T. M., & Lavallée, D. (2000). Multifractal versus monofractal analysis of wetland topography. *Stochastic Environmental Research and Risk Assessment*, *14*(1), 8–32. https://doi.org/10.1007/s004770050002

Weissel, J. K., Pratson, L. F., & Malinverno, A. (1994). The length-scaling properties of topography. *Journal of Geophysical Research*, *99*(B7), 13,997–14,012. https://doi.org/10.1029/94JB00130

Welch, P. D. (1967). The use of fast Fourier transform for the estimation of power spectra: A method based on time averaging over short, modified periodograms. *IEEE Transactions on Audio and Electroacoustics, AU*, *15*(2), 70–73.

Wendt, H., Roux, S. G., Jaffard, S., & Abry, P. (2009). Wavelet leaders and bootstrap for multifractal analysis of images. *Signal Processing*, *89*(6), 1100–1114. https://doi.org/10.1016/j.sigpro.2008.12.015

Wooding, R. A., Bradley, E. F., & Marshall, J. K. (1973). Drag due to regular arrays of roughness elements of varying geometry. *Boundary-Layer Meteorology*, *5*(3), 285–308. https://doi.org/10.1007/BF00155238

Yu, X., Rosman, J. H., & Hench, J. L. (2018). Interaction of waves with idealized high-relief bottom roughness. *Journal of Geophysical Research: Oceans*, *123*, 3038–3059. https://doi.org/10.1029/2017JC013515

Zawada, D. G., & Brock, J. C. (2009). A multiscale analysis of coral reef topographic complexity using lidar-derived bathymetry. *Journal of Coastal Research*, *53*, 6–15. https://doi.org/10.2112/SI53-002.1

References From the Supporting Information

Arneodo, A., Audit, B., Decoster, N., Muzy, J. F., & Vaillant, C. (2002). Wavelet based multifractal formalism: Applications to DNA sequences, satellite images of the cloud structure and stock market data. In A. Bunde, J. Kropp, & H. J. Schellnhuber (Eds.), *The science of disasters: Climate disruptions, heart attacks, and market crashes*, (pp. 26–102). Berlin, Germany: Springer. https://doi.org/10.1007/978-3-642-56257-0_2

Lovejoy, S., & Schertzer, D. (2007). Scaling and multifractal fields in the solid earth and topography. *Nonlinear Processes in Geophysics*, *14*(4), 465–502. https://doi.org/10.5194/npg-14-465-2007

Wendt, H., Abry, P., & Jaffard, S. (2007). Bootstrap for empirical multifractal analysis. *IEEE Signal Processing Magazine*, *24*(4), 38–48. https://doi.org/10.1109/MSP.2007.4286563